Evaluation of cloud properties from the reanalysis over East Asia with a radiance-based approach

Bin Yao[1,2], Chao Liu[1,2], Yan Yin[1,2], Zhiquan Liu[3], Chunxiang Shi[4], Hironobu Iwabuchi[5], and Fuzhong Weng[6]

[1]Collaborative Innovation Center on Forecast and Evaluation of Meteorological Disasters, Nanjing University of Information Science & Technology, Nanjing 210044, China

[2]Key Laboratory for Aerosol-Cloud-Precipitation of China Meteorological Administration, School of Atmospheric Physics, Nanjing University of Information Science & Technology, Nanjing 210044, China

[3]National Center for Atmospheric Research, Boulder, CO 80301, USA

[4]National Meteorological Information Center, China Meteorological Administration (CMA), Beijing 100081, China

[5]Center for Atmospheric and Oceanic Studies, Graduate School of Science, Tohoku University, Sendai, Miyagi 980-8578, Japan

[6]Chinese Academy of Meteorological Sciences, Beijing 100081, China

Correspondence to: Chao Liu (chao_liu@nuist.edu.cn)

Abstract. Extensive observational and numerical investigations have been performed to better characterize cloud properties. However, due to the large variations of cloud spatiotemporal distributions and physical properties, quantitative depictions of clouds in different atmospheric reanalysis datasets are still highly uncertain. A radiance-based evaluation approach is introduced and performed to evaluate the quality of cloud properties from the reanalysis. The China Meteorological Administration Reanalysis (CRA), ECMWF's Fifth-generation Reanalysis (ERA5), and Modern-Era Retrospective Analysis for Applications, Version 2 (MERRA-2), i.e., those providing sufficient cloud information, are considered. To avoid the influence of assumptions and uncertainties on satellite retrieval algorithms, forward radiative transfer simulations are used as a bridge to "translate" the reanalysis to corresponding radiances that are expected to be observed by satellites. The simulated reflectances and brightness temperatures (BTs) are directly compared with observations from the Advanced Himawari Imager onboard the Himawari-8 satellite in the East Asian region. We find that the simulated reflectances and BTs based on CRA and ERA5 are close to each other. CRA better represents the total and mid-layer cloud cover than other two datasets, and ERA5 depicts deep convection structures more closely than CRA. Comparisons of the simulated and observed BT differences suggest that water clouds are generally overestimated in ERA5 and MERRA-2, and MERRA-2 also overestimates the ice clouds over the cyclones centers. Overall, clouds from CRA, ERA5, and MERRA-2 show their own advantages in different aspects. The ERA5 reanalysis has the best capability in representing the cloudy atmospheres over East Asia, and the CRA representations are close to those in ERA5.

1 Introduction

As an important element in the Earth atmosphere, clouds play a vital role in the global radiation budget, water cycle, and climate change. Cloud formation is governed by the balance between dynamical, thermodynamic, and microphysical processes (Boucher et al., 2013). Although the representations of clouds and cloud evolution in regional and global models have been significantly improved in the past few decades (Cess et al., 1989; Cotton et al, 2003; Arakawa, 2004), cloud is still one of the dominant uncertainties in the atmosphere, and causes difficulties in understanding the energy budget and climate change (Dufresne and Bony, 2008; Boucher et al., 2013).

The atmospheric reanalysis, a dataset that combines observations and forecasting products (Dee et al., 2011), provides multivariate records of the global atmospheric circulation, and is widely used in the studies of climate change, initialization of numerical models, and satellite retrievals. With the advances in computation capability and the improvement of global observing systems, an increasing number of observed datasets are assimilated into the reanalysis by more advanced data assimilation methods and systems, and the reanalysis is being closer to realistic atmospheres. A series of reanalysis data have been produced, for example, the National Centers for Environmental Prediction (NCEP) 40-yr Reanalysis Project (Kalnay et al., 1996), the 40-year ECMWF Reanalysis (Uppala et al., 2005), the Japanese 25-year Reanalysis (Onogi et al., 2007), the Modern-Era Retrospective Analysis for Research and Applications (Rienecker et al., 2011), the ECMWF's Interim Reanalysis (Dee et al., 2011), and the Japanese 55-year Reanalysis (Kobayashi et al., 2015). Some schemes and systems that support the assimilation of cloud-affected satellite radiance are developed (Chevallier et al., 2004; MaNally, 2009). However, it is still difficult to assimilate cloud information into the reanalysis, instead, they are forecasted by numerical weather prediction models (Free et al., 2016). Thus, most atmospheric parameters in the reanalysis are increasingly confident, but the representation of clouds is still challenging. Actually, it is important yet difficult to accurately and reasonably evaluate the cloud properties in different atmospheric reanalysis datasets.

Because of large spatial and temporal coverages, the satellite observation is one of the best choices in the evaluation of output fields from numerical models. Some previous studies have conducted evaluations of reanalysis or model outputs based on satellite retrieved products. This is known as the satellite- or retrieval-based approach. Interesting results are achieved by this method (Jakob, 1999; Waliser et al., 2009; Hashino et al., 2013), especially for the long-term cloud cover in the reanalysis. However, some evaluations by the retrieval-based approach may be questionable due to the nature of retrieval products (Matsui, et al., 2014). Assumptions are needed to infer unknown quantities, and this will introduce inevitable uncertainties on the retrieval results. For example, the cloud vertical profile is one of the most essential properties in most models, cloud optical and microphysical properties from the radiometer retrievals are normally based on single-layer and homogeneous assumption (Wind et al., 2013; Yang et al., 2015). The average relative differences of ice optical depth retrieved by Advanced Himawari Imager (AHI)/Himawari-8 and collocated Moderate Resolution Imaging Spectroradiometer (MODIS) are as large as 40% (Lai et al., 2019), and even MODIS products from different collections show significant differences (Yi et al., 2017a; 2017b). Among various assumptions, the scattering properties of cloud particle

models themselves are with significant uncertainties, and they are inconsistence in different retrieval approaches. Yi et al. (2017a; 2017b) indicate that any mismatch in cloud optical parameterizations or retrieval algorithms could induce large biases in the retrievals.

Because directly quantitative or qualitative evaluations are straightforward, the retrieval-based evaluation is an indispensable but questionable approach in the evaluation of atmospheric properties from various simulations. However, to avoid uncertainties associated with satellite retrieval algorithms, an alternative radiance-based comparison is introduced for the evaluation in our study. In this approach, simulated radiative parameters, such as brightness temperature (BT) in the infrared (IR) channels or microwave channels and reflectance in the solar channels, are first calculated by a forward radiative transfer model (RTM), and calculated radiative variables are then compared with satellite radiative observations directly, i.e., no retrieval involved. In order words, the RTMs, not the retrievals, build a bridge between modeled atmospheric parameters (e.g., those from the reanalysis dataset) and satellite observations (Zhang et al., 2019). This will effectively avoid frustration from the uncertainties of satellite retrieval algorithms. The method was applied to evaluate simulated cloud fields using in the thermal IR observations by Morcrette (1991) and Yu et al. (1991). With the advantages of confident radiative information and the diversity of satellite observations, the radiance-based method has been applied to evaluate different cloud microphysics schemes (Han et al., 2013, Yao et al., 2018), precipitation microphysics schemes (Hashino et al., 2013), and even aerosol properties (Chaboureau et al., 2007), and became an important way to better understand the microphysical and radiative properties of clouds, precipitation, and other atmospheric parameters.

This study extends the application of radiance-based approach to evaluate the cloud properties in three reanalysis datasets: the China Meteorological Administration Reanalysis (CRA), the ECMWF's Fifth-generation Reanalysis (ERA5; Hersbach and Dee, 2016) and the Modern-Era Retrospective Analysis for Research and Applications, Version 2 (MERRA-2; Gelaro et al., 2017). This is a new aspect to evaluate cloud and atmosphere properties from different atmospheric reanalysis. The radiative observations from AHI onboard the Himawari-8 satellite (Bessho et al., 2016) are used as the "truth".

This paper is organized as follows. The datasets are introduced in Section 2. The method for the couple of cloud microphysical parameters in the reanalysis and radiative variables in RTM are described in Section 3. A detailed radiance-based evaluation on cloud properties from the reanalysis, including a case assessment and a long-term comparison, is presented in Section 4. Section 5 summarizes the study.

2 Dataset

The newly developed Chinese first-generation atmospheric reanalysis CRA uses the National Oceanic and Atmospheric Administration Global Forecast System model and Gridpoint Statistical Interpolation 3-Dimensional Variation Analysis data assimilation system (Wu et al., 2002; Kleist et al., 2009) with a T574 spectral resolution (34 km grid spacing). The final CRA product will span the period from 1979 to 2019, and be produced and released in late 2020. An interim version of CRA (CRA-interim) for a 10-year period (between 1 January 2007 and 31 December 2016) at a 6-hourly time interval was

produced in February 2018. An abundance data from in-situ observations and multiple satellite instruments, especially for the East Asian regions, have been assimilated into CRA-interim. More than 50 kinds of satellite observations, e.g., microwave radiance from TOVS, ATMS, and MWHS, IR radiance from IASI and CrIS, ocean wind data from MetOp and SSM/I, and the atmospheric motion vector data from GOES, MTSAT, Himawari-8, MODIS, and AVHRR, are considered (Wang et al., 2018). Meanwhile, a large amount of Chinese surface and radiosonde datasets are assimilated into CRA (Liao et al., 2018). Those improvements significantly enhance the capability of CRA in reproducing realistic atmospheres over Asia. CRA-interim has 47 pressure levels from the surface to 0.27 hPa with a horizontal resolution of 0.3125° × 0.3125°.

ERA5 is one of the latest released numerical datasets of the recent climate. It is available for the period from 1979 to present, and will be extended from 1950 to present. Satellite observed BTs from AMSRE, SSM/I, SSMIS, and TMI are assimilated for the cloud liquid water, column water vapor, and humidity sensitivities analysis, and BTs from GOES IMAGER, SEVIRI, MVIRI, and AHI are used for the analysis of water vapor and surface/cloud top temperature. The spatial resolution of ERA5 is 0.25° × 0.25°, and the atmospheric data has 37 pressure levels from the surface to 1 hPa (Hersbach and Dee, 2016).

MERRA-2 is produced by the NASA Global Modeling and Assimilation Office with the Goddard Earth Observing System atmospheric data assimilation system. It provides data from 1980 to present and is designed to build a bridge between the first MERRA reanalysis and the long-term goal of developing an integrated Earth system analysis (Gelaro et al., 2017). Compared with MERRA reanalysis, microwave and IR radiances from ATOVS and ATMS, hyperspectral IR radiances from IASI and CrIS, and the radiances from geostationary MSG SEVIRI and GOES satellites (GOES-11, GOES-13, and GOES-15) are considered. MERRA-2 is at a spatial resolution of 0.5° × 0.625° with 42 pressure levels from the surface to 0.1 hPa.

To evaluate the quality of the three reanalysis datasets, satellite observations from AHI/Himawari-8 are used. Launched on 7 October 2014 and operated by the Japan Meteorological Agency since 2015, the Himawari-8 is one of the new generation satellite members of the Multi-functional Transport Satellites. AHI radiometer include 16 bands from the solar to IR, and we consider observations within the region from 80° E to 160° W and between 60° N and 60° S. The spatial resolution is 0.5–2 km at nadir, and the temporal resolution is 2.5–10 minutes (Bessho et al., 2016; Iwabuchi et al., 2018). The full disk data we used is at a spatial resolution of 0.05° × 0.05°.

All reanalysis datasets used in this study are at a 6-hourly time interval (4 time steps each day), and the spatial resolutions are re-gridded to that of CRA by the inverse distance weighted method (Guan and Wang, 2007; Holz et al., 2008). An 8-day case and a general comparison with 36-day data (total of 144 realizations) spanning one year are considered. Although the size of the evaluated datasets is small, the statistically credible results are presented.

3 Methodology

We focus on clouds in the reanalysis, so one of the most critical factors for the reliability of the evaluation is the treatments on cloud properties. Cloud effective radius (R) and optical depth (τ) are key parameters in determining the radiative properties in each atmospheric layer in the RTM. This means that cloud mixing ratio (q_c), i.e., variables from the reanalysis, cannot be directly considered by the fast RTM. A reasonable coupling method between the cloud properties provided by the

reanalysis and the optical parameterizations used by the RTM has to be developed first, and we try to make the coupling approach with less empirical assumptions. Table 1 lists the geophysical parameters in the reanalysis that are used in our study. In each grid box, the occurrence of cloud is diagnosed with a criterion of the cloud mixing ratio being larger than 0.001 g/kg. For cloud phase, if the temperature of cloud layer is larger than 253 K, then the grid box is defined as a water cloud layer, otherwise the grid box is regarded as an ice cloud layer (Mazin, 2004). Noted that by using a single criterion of 253 K, the mixed-phase clouds within a single layer is not considered. We have verified that it would introduce little bias in the simulated BT/reflectance. Then, R and τ are approximated based on cloud mixing ratio q_c of the grid layer.

If the layer is determined to be a water cloud layer, the water effective radius (R_w) is approximated by q_c and number concentration (N_w) (Thompson et al., 2004):

$$R_w = \frac{1}{2} \times \left(\frac{6\rho_a q_c}{\pi \rho_w N_w}\right)^{\frac{1}{3}} \quad (1)$$

where ρ_a is the density of air, which is determined by the pressure and temperature in the corresponding layer. The density of water cloud particles (ρ_w) is 1000 kg/m^3. A water cloud number concentration over the continent of $N_w = 3 \times 10^8$ m^{-3} is assumed, and $N_w = 1 \times 10^8$ m^{-3} is used for water clouds over the ocean region (Miles et al., 2000).

The approximation for ice clouds are slightly different. The ice cloud effective radius (R_i) is obtained by the relationship between mass extinction coefficient (k) in the visible wavelength and cloud effective radius. The k can be given by an empirical relationship based on in-situ measurements (Heymsfield and McFarquhar, 1996; Platt, 1997; Heymsfield et al., 2003):

$$k = 0.018 \times (\rho_a q_c)^{-0.14} \quad (2)$$

Once k is obtained, the corresponding R_i can be calculated because k is parameterized as a function of R_i in the framework of some RTM.

The optical depth is the other key radiative parameter in the RTM. When the cloud effective radius (R_w *or* R_i) and the corresponding k are given, the cloud optical depth in the visible wavelength can be obtained by:

$$\tau = k \times \rho_a \times q_c \times \Delta h \quad (3)$$

where Δh represent the height of the cloud layer. Again, here τ is the optical depth at the reference wavelength, and that at the specific instrumental channel is converted in the RTM simulations.

The Community RTM (CRTM) is used to calculate satellite observed radiative variables based on the atmospheric variables from the reanalysis. The model is designed to simulate radiance and radiance gradients at the top of atmosphere, and has been widely applied in radiance assimilation, remote sensing calibration, climate reanalysis and so on. Procedures for solving the radiative transfer in the model are divided into various independent modules (e.g., gaseous absorption module, surface emissivity module, and cloud absorption/scattering module) (Chen et al., 2008; Ding et al., 2010). To improve the computational efficiency, the advanced fast adding-doubling method is used (Liu and Weng, 2006), and it is 1.7 times faster than the vector discrete ordinate method (Weng, 1992) and 61 times faster than the classical adding-doubling method (Twomey et al., 1966; Hansen and Hovenier, 1971). Four major surface types (i.e., water, land, ice, and snow) are included

in the surface emissivity module, and the corresponding spectral library from visible to microwave wavelengths is pre-prepared for the emissivity calculation (Chen et al., 2008; Baldridge et al., 2009).

To minimize the numerical errors and uncertainties from radiative transfer computation, the cloud optical property look-up tables in the absorption/scattering module of CRTM are updated before the simulation. We calculate the single-scattering optical properties of water clouds by Lorenz-Mie theory (Mie, 1908). The single-scattering optical properties of ice clouds are from the data library developed by Yang et al. (2013), and use those based on aggregate columns with eight elements and severely roughened surface, which is found to better represent actual ice cloud properties (Järvinen et al., 2019). Gamma size distributions with an effective variance of 0.1 (Hansen and Travis, 1974) are assumed to give the bulk scattering properties. Validation of the CRTM with the new optical property look-up tables is presented in Yao et al. (2018), and the BT differences (BTDs) between the CRTM and rigorous models in different channels are generally less than 1 K for ice clouds. For water clouds, the biases in the IR window channels may reach to 2 K for optical thin clouds. BTDs in the water vapor channels are within ±1 K. Moreover, compared to the default CRTM model, the updated model can substantially improve CRTM simulations on cloudy atmospheres (Yi et al., 2016; Yao et al., 2018).

To obtain the most realistic representation of the radiance from the top of atmosphere, the full layer atmospheric profiles (i.e., pressure, temperature, and water vapor) and cloud mixing ratio are kept and adopted by CRTM. The surface characteristics (e.g., surface type, altitude, and surface temperature) are necessary for the CRTM to give the surface radiative property and they are also given by the atmospheric reanalysis directly. Because the ozone absorption is insensitive in the channels of interest, the climatological ozone profiles are used in the simulation.

It should be noted that schemes for both cloud optical properties (e.g., cloud model) in the RTM and the coupling between atmospheric reanalysis and RTM (e.g., approximation of cloud effective radius) may influence simulated BT/reflectance. However, the influences are relatively minor compared to the presences of clouds (cloud amount), so the potential numerical uncertainties due to different schemes will be performed with more details in the future studies.

4 Evaluation of the reanalysis

4.1 Case evaluation

We first present an evaluation of the cloud properties in three reanalysis datasets based on a typical case from 10 to 17 September 2016. The super typhoon Meranti, one of the most powerful tropical cyclones on record, was monitored during the period. The particular atmospheric environment, e.g., adequate water vapor, increased outflow in the upper layer, and warm sea surface temperature, intensified the structure and energy of the typhoon. Meanwhile, on 11 September 2016, another tropical depression was detected and monitored over the Northwest Pacific Ocean, and it evolved into the typhoon Malakas on 13 September. The interaction between the two typhoons increased the water vapor transportation, promoted the development of deeper and thicker clouds, and enhanced them (Zhou and Gao, 2016). Note that even for this case study, we consider a period over eight days covering 32 time steps.

Figure 1 shows the spatial distribution patterns of the reflectance in the 0.64- and 1.6-μm channels. The observed and simulated results are taken at 00:00 UTC on 12 September 2016. Four typical regions (A to D) marked by red boxes are chosen for further discussions. In these two channels, atmospheric profiles have little effect on the simulated reflectance, and the differences are mainly contributed by cloud properties. Because clouds are non-absorbing the 0.64-μm visible channel, the reflectance is primarily constrained by the cloud optical depth. Therefore, some cloud macro characteristics can be recognized from the result in this channel. The pixels with reflectance close to 1 (the whiter ones) indicate the region covered by optically thick clouds. Comparing to the observation, CRA represents the cloud spatial distribution more reasonably than ERA5 and MERRA-2. ERA5 and MERRA-2 obviously overestimate the cloud cover, especially over the ocean regions, e.g., regions B and C. Because ice particles absorb stronger than water droplets with the same optical depth in the 1.6-μm channel, the reflectance in this channel is usually smaller for pixels covered by ice clouds than those covered by water clouds (Wang et al., 2018). Thus, the comparison in the 1.6-μm channels can also briefly illustrate the representation of cloud phase. Comparing the results over region B, the three reanalysis datasets all represent the cloud phase characteristics of cyclones. Larger reflectance values from ERA5 suggest that overestimated clouds are from water phase clouds, but the overestimation in MERRA-2 are mostly attributed to ice clouds. For pixels over regions C and D, ERA5 and MERRA-2 both overestimate water clouds.

To give a quantitative evaluation of the results in Figure 1, the pixel-to-pixel comparisons of the case are shown in Figure 2. The color contours show the occurrence of the reflectance from the corresponding observations and simulations, and the color bar is shown on a logarithmic scale. For CRA, high occurrence frequencies occur around the black 1:1 line, confirming that CRA has a better agreement with the observed reflectance than ERA5 and MERRA-2. The correlation coefficients between observations and CRA-based simulations are 0.66 and 0.62 in the 0.64- and 1.6-μm channels, respectively, revealing the best simulation in the solar channels. The ERA5-based and MERRA-2-based reflectances are clearly larger than the observed ones in a large number of pixels, and high occurrence frequencies also noticed near the x-axis, i.e., pixels with observed reflectance less than 0.1 but simulated up to 0.6. These higher occurrence frequencies correspond to the overestimated cloud pixels. The correlation coefficients for ERA5 and MERRA-2 are 0.65 and 0.53, respectively, in the 0.64-μm channel, and become less than 0.5 in the 1.6-μm channel.

Different from the reflectance in the solar channels, BTs in the IR channels are available for both daytime and nighttime. For further evaluation, the discussions are mostly based on the results in three IR channels (one in the 6.2-μm water vapor channel, and two in the IR window channels). Figure 3 illustrates the observed BTs in the 6.2-, 8.6-, and 11.2-μm channels, and the BTDs between the simulations from CRA, ERA5, and MERRA-2 and the observations (here, BTD = simulated BT – observed BT). Results are taken at 00:00 UTC on 12 September 2016, the same as Figure 1. Gas molecular absorption in the two IR window channels (8.6- to 11.2-μm) is ignorable, so the two channels are mostly sensitive to the surface temperature and cloud profiles. Therefore, the BTs in these channels are usually used to evaluate cloud properties or surface temperature (King et al., 1992; Mao et al., 2005). In the 6.2-μm channel, because of large sensitivity to a broad upper-layer humidity, the BTs are used to infer the mid- to high-layer water vapor content. Similar distributions between the observation and

simulation in the two IR window channels generally confirm the dependable capabilities of the three reanalysis datasets to represent the atmospheric characteristics on both cloudy and clear-sky pixels. The smallest average BTD between the simulated BT and observed BT over the entire region is -1.59 K in the 11.2-μm channel for ERA5, and the average results for CRA are close to it. However, the mean BTD between MERRA-2-based simulation and observation is as large as -9.19 K, indicating the relatively poor performance of MERRA-2 over the region. Region A (a continental region) is characterized by low-layer clouds or clear-sky conditions, and the mean BTDs over the region are 1.56 K for CRA, 1.00 K for ERA5, and -5.35 K for MERRA-2. The slight underestimation on cloud optical depth or cloud top height over this region causes the positive mean BTDs for CRA and ERA5, and the negative mean BTD for MERRA-2 indicates that clouds (optical depth or top height) are overestimated. Over region B, clouds in the reanalysis, i.e., pixels with simulated BTs between 220 and 250 K, are largely responsible for the negative BTDs. The absolute BTDs may reach as large as 80–90 K, and the mean values are almost 15–20 K larger than those over region A. More series excessive cloud pixels for MERRA-2 explain the mean BTD of -19.02 K in the 11.2-μm channel. The negative mean BTDs over region B for CRA and MERRA-2 in the 6.2-μm channel suggest the excessive integrated mid- to high-layer water vapor content. The positive mean BTD (the 6.2-μm channel) for ERA5 over region B reveals a general insufficient water vapor content over the corresponding layer, and this results in the underestimation of upper-layer clouds. Meanwhile, the mean BTD of -2.35 K in the 11.2-μm channel indicates that the overestimation of clouds should be related to low- or mid-layer clouds in this region. However, more water vapor content is represented in ERA5 over region C than that in CRA and MERRA-2, and it is closer to the realistic atmosphere. Compared with the observation, a similar cyclone structure is captured in the imagery of IR window channel, i.e., much better than the solar channel results. However, other atmospheric or surface properties may also cause similar results over the arid or semiarid regions, and the limitation of the in-situ observations over the Tibetan Plateau also enlarges uncertainties for the reanalysis datasets. Compared with the continental regions, larger simulation errors over ocean are associated with more complex cloud distributions as well as less observations assimilated.

Figure 4 gives a similar pixel-to-pixel evaluation to Figure 2 but for the results in the IR channels. The correlation coefficients between observations and simulations are all larger than 0.6, and the high occurrences are distributed around the 1:1 line, revealing good agreements between the simulated and observed BTs in the 11.2-, 8.6-, and 6.2-μm channels, especially for CRA and ERA5.

To better understand the representations on cloudy and clear pixels, we classify the simulated pixels based on an integrated column cloud optical depth of 0.001 ($\tau > 0.001$ as cloudy pixels, and $\tau < 0.001$ as clear pixels), and upper and lower panels of Figure 5 compare observed and simulated BTs in the 11.2-μm for cloudy and clear cases, respectively. The upper panels show clearly wider distributions on the occurrence frequency and smaller correlated coefficients between observations and simulations, and this means that the cloud representation definitely introduces additional errors to the simulated BTs. Particularly for MERRA-2, much larger correlated coefficient for the clear pixels indicate that cloud property representation in MERRA-2 may significantly contribute to the differences from the observations.

Figure 6 shows the probability (top panels) and cumulative probability (bottom panels) of the simulated and observed reflectance and BT with particular values. Taken the IR channel BT as an example, the probability and cumulative probability are numerically calculated as:

$$Probability\ (BT_o) = \frac{Number\ of\ pixels\ with\ BT\ between\ [BT_o - \Delta BT,\ BT_o + \Delta BT]}{Total\ pixel\ number} \quad (4)$$

and:

$$Cumulative\ Probability\ (BT_o) = \frac{Number\ of\ pixels\ with\ BT\ less\ than\ BT_o}{Total\ pixel\ number} \quad (5)$$

In the IR window channels, MERRA-2 overestimates the probability against the observation between 220 and 275 K, reflecting the overestimation of mid- and mid-to-high layer cloud. For ERA5, the low-layer clouds are overestimated, but the high-layer clouds are underestimated, especially for clouds with a top temperature less than 230 K. Compared to CRA and MERRA-2, similar probability density structures between the ERA5-based simulation and observation in the 6.2-μm channel reveal a more reasonable water vapor distribution over the entire region. If a threshold of BT ~ 275 K in the 11.2-μm channel is assumed to defined cloud pixels, the simulated cloud cover for CRA reanalysis achieves the best agreement with the observation. However, cumulative probability densities with BTs of ~ 275 K in ERA5 and MERRA-2 are larger than the corresponding values given by the observation, indicating an overestimation of cloud cover in the two datasets.

The atmospheric and cloud profiles (i.e., temperature, cloud effective radius and optical depth) over pixels of 18°N (marked by blue solid lines in Figure 3) are shown in Figure 7. Compared with the differences of temperature profiles, the differences on the cloud effective radius and optical depth are more obvious. Clouds in the CRA are developed insufficiently over the low-to-mid layer compared to the ERA5 and MERRA-2. Abnormally widespread cloud profiles or excessive integrated cloud optical depth in the mid- to high-layers bring in lower simulated BTs in the IR channels, and this is significant over the Region D in Figure 3.

Different spectral channels have their own sensitivities to atmospheric and cloudy properties, so different cloud properties or atmospheric conditions can be detected and validated by the BTDs among different channels (Baum et al. 2000; Otkin et al. 2009). Different from previous analysis based on single channel results, Figure 8 shows the observed and simulated BTDs of 8.6 – 11.2-μm (top panels) and 6.2 – 11.2-μm (bottom panels). The absorptivity of different phase clouds is similar in the 8.6-μm channel, but the absorption of ice clouds is larger than that of water clouds in the 11.2-μm channel. Thus, in typical cases, the 8.6 – 11.2-μm BTDs are positive for ice clouds and negative for water clouds. In region A, simulations for CRA are close to the observations, and the mean BTDs are both around 0.15 K. The negative mean BTDs in this region for ERA5 and MERRA-2 indicate an overestimation of water clouds or underestimation of ice clouds. Because of the strong water vapor in the 6.2-μm channel and the negative temperature lapse rate in the troposphere, the BTDs of 6.2 – 11.2-μm are usually negative, and they increase as the cloud height increases. The largest negative BTDs are often in the clear-sky region with sufficient water vapor and high surface temperature, and the positive or near zero BTDs correspond to overshooting cloud tops. Although the simulation for ERA5 reanalysis generally underestimates the mid- to high-layer water vapor content and upper-layer cloud in entire and A region, as we mentioned before, if we isolate the overshooting cloud top by

BTDs less than 0 K, the ERA5 has the closest structure and distribution to the observation over the three reanalysis datasets, corresponding to the analysis of region B.

The results discussed above are from a single time step, and the following gives a more general evaluation of the cloud cover in the 8-day case. The BTD between 6.2- and 11.2-μm channels is used to classify pixels with clouds over different altitudes (Mecikalski and Bedka, 2006; Yao et al., 2018). Pixels with BTDs between -45 and -30 K are understood as low-layer clouds, and we define the "Low-layer cloud ratio" as:

$$Low\text{-}layer\ cloud\ ratio = \frac{Number\ of\ pixels\ with\ simulated\ BTD\ between -45\ and -30\ K}{Number\ of\ pixels\ with\ observed\ BTD\ between -45\ and -30\ K} \quad (6)$$

Similarly, we have the "mid-layer cloud ratio" defined with BTDs between -30 and -10 K, and the "high-layer cloud ratio" given by pixel numbers with BTDs larger than -10 K. Note that the ratios here are those of simulated pixels to observed pixels with particular BTD, so ratios close to 1 indicate better performance of the cloud representation. The ratios as a function of time are illustrated in Figure 9. The CRA total cloud cover (TCC) ratio and mid-layer cloud ratio are close to 1. The low-layer cloud ratio for MERRA-2 reanalysis is reasonable, but large mid- and high-layer cloud ratios (~ 1.6 and ~ 2) result in a substantial overestimation of TCC by ~ 30%. For ERA5, the high-layer cloud ratio is approximately 0.7, and the low- and mid-layer cloud ratios are both larger than 1.

4.2 Long-term evaluation

A long-term case spanning in an entire year of 2016 is chosen to give a more general idea on reanalysis clouds, and we consider 144 realizations, i.e., 4 time steps per day (6-hourly time interval for all reanalysis), 3 days per month (5^{th}, 15^{th}, and 25^{th}), and 12 months. The size of the dataset is not large enough, but the significant characteristics are presented.

Similar to Figure 9, Figure 10 gives the ratio of clouds over the 144 realizations, and the average values are listed in Table 2. For CRA and ERA5, the ratios of clouds show relatively weak variation over time, and the means and variations are both similar to the results in Figure 9. Clear seasonal variation is noticed for the bias of MERRA-2 cloud representation. Such seasonal variations are only shown for mid-layer clouds of ERA5, and are not shown for CRA. The simulated mid-, high-layer cloud ratios in MERRA-2 in summer are significantly larger than those in other seasons.

Figure 11 illustrates the BTDs between the simulations and the observations in the 11.2-, 8.6-, and 6.2-μm channels, averaged over the results from the 144 time steps. Over the entire region, most pixels have average BTDs around 0 K in the IR window channels, which reveals good representations in CRA and ERA5. Regions with larger deviations are generally over the arid or semiarid areas (as marked by region A in Figure 3), and the surrounding regions of the equator. For MERRA-2, there are significant deviations with negative BTDs over the Intertropical Convergence Zone, and the phenomenon is extended to the region around 20° N. Most pixels of positive BTDs in the water vapor channel for ERA5 indicate an underestimation of water vapor, and it is more obvious over the Intertropical Convergence Zone.

Figure 12 shows the temporal variation of the mean BTDs (MBTD, i.e., average of the BTDs between simulation and observation over the entire interested region), standard deviations of the BTDs (SBTD, i.e., corresponding standard deviation

of the BTDs over the whole region), and correlation coefficient (R, correlation coefficient between simulated and observed BTs) in the 11.2-, 8.6-, and 6.2-μm channels, and the corresponding average values are listed in Table 2, together with the results for Figure 10. Three statistical parameters show seasonal variation characteristics over time and the largest errors are in northern hemisphere's summer time because of more complex weather systems and clouds. The mean BTDs for the three reanalysis datasets are always negative in the 11.2- and 8.6-μm channels, demonstrating the general overestimation of clouds, especially for MERRA-2 in summer. In the 6.2-μm channel, the opposite phases of mean BTDs indicate the general underestimated mid- to high-layer water vapor for ERA5 but an overestimation for CRA, corresponding to the analysis in Figure 11.

Overall, the spatial distributions of the average BTDs in Figure 11 and the statistical evaluation in Figure 12 indicate that the results for ERA5 have the best capability to represent atmospheric and cloud characteristics over the corresponding large region of Himawari-8 observation, with the smallest absolute mean BTD of 0.92 K, the smallest standard deviation of BTDs of 12.77 K, and the largest correlation coefficient of 0.80. The CRA results are close to those in ERA5, whereas the deviations are slightly larger for MERRA-2. Large and systemic deviations for the three reanalysis are mostly over the oceanic region around the equator and areas with complex surface features. This is because that the atmospheric and cloud characteristics are complex and volatile, and the in-situ observations are limited over these regions.

5 Summary

This study performs an evaluation of cloud properties from three reanalysis datasets (i.e., CRA, ERA5, and MERRA-2) with the Himawari-8 satellite observation by the radiance-based approach. The atmospheric and cloud variables in the reanalysis are converted into BTs or reflectance with the help of the coupling between the reanalysis and RTM (i.e., CRTM), and the simulated radiative values are compared and analysed with the direct satellite observations.

The atmospheric and cloud characteristics from CRA, ERA5, and MERRA-2 are mostly represented. The BTs in the IR window channels (i.e., 11.2- and 8.6-μm) and reflectance in the 0.64-μm channel reveal the excellent TCC and mid-layer cloud in CRA. For MERRA-2, the low-layer clouds are more reasonable than clouds over other layers, and the widespread overestimated TCC is mostly caused by the overestimation of mid- and high-layer clouds. The reflectances in the 1.6-μm channel and the BTDs of 8.6 – 11.2-μm reflect the overestimated water vapor pixels over the ocean region in ERA5 and MERRA-2. However, it is slightly different over the center of the cyclone because more ice cloud pixels are depicted in MERRA-2.

Generally, the CRA, ERA5, and MERRA-2 are all capable for representing the atmospheric and cloud characteristics over the Himawari-8 observed region. The larger statistical errors occur over the oceanic region around the equator and areas with complex surface features, because of the complex atmospheric and cloud structures, and the limitation of in-situ observations that can be assimilated into the reanalysis. The largest correlation coefficients of 0.80 and 0.90 between the observations and simulations in the IR window and water vapor channels, respectively, demonstrating that ERA5 achieves the generally best accuracy. The results for CRA also reveal reasonable simulations, and they are close to those in ERA5, whereas for

MERRA-2, the deviations are slightly larger. It should be noticed that both ERA5 and CRA reanalysis consider the Himawari-8 observation for assimilation (see Section 2), whereas the MERRA-2 does not. This may be one of the reasons that MERRA-2 has relatively poor performance on cloud representation over the East Asia.

Compared with the evaluation by satellite retrieved cloud products, the direct comparison of radiative parameters provides a more reasonable evaluation of the microphysical and radiative properties of the atmospheric and cloud properties from the reanalysis. It effectively avoids uncertainties associated with satellite retrieval, such as the scattering properties of cloud model, retrieval algorithms, and platforms. Meanwhile, there are also some drawbacks for the radiance-based model that should be considered in future studies. For examples, differences between simulated and observed radiances can be contributed by both cloud and atmospheric variables, which can hardly be separated, and these may be distinguished by considering the same atmospheric profiles in the RTM simulation. Last but not least, although the focus of this manuscript is on the observed region of Himawari-8 satellite and cloudy atmospheres, this approach can be applied for more parameters (e.g., cloud, aerosol, precipitation, and so on) over any region with satellite observations available. Furthermore, the radiance-based evaluation should also be possibility to be used to the improvement of cloud properties in the reanalysis as well as in regional or global models, and to the design of observations.

Data availability.

The data in this study are available at: https://github.com/carrolyb/Reanalysis_Evaluation_2019/.

Author Contributions.

BY and CL designed the study, carried out the research, and performed data analysis. BY, CL, YY, ZL, CS, HI, and FW discussed the results and wrote the paper. All authors gave approval for the final version of the paper.

Competing interests.

The authors declare that they have no conflict of interest.

Acknowledgements.

We acknowledge funding supported by the Special Fund for Meteorological Scientific Research in Public Interest (GYHY 201506002), the National Natural Science Foundation of China (NSFS, grants 41975025 and 41590873), and the Postgraduate Research & Practice Innovation Program of Jiangsu Province (KYCX18_1004). The computation is supported by the National Supercomputer Center in Guangzhou (NSCC-GZ).

References

Arakawa, A.: The cumulus parameterization problem: Past, present, and future, J. Climate, 17, 2493-2525, https://doi.org/10.1175/1520-0442(2004)017<2493:RATCPP>2.0.CO;2, 2004.

Baldridge, A. M., Hook, S. J., Grove, C. I., and Rivera, G.: The ASTER spectral library version 2.0. Remote Sens. Environ., 113, 711-715, https://doi.org/10.1016/j.rse.2008.11.007, 2009.

Baum, B. A., Kratz, D. P., Yang, P., Ou, S. C., Hu, H., Soulen, P. F., and Tsay, S.-C.: Remote sensing of cloud properties using MODIS airborne simulator imagery during SUCCESS.I. Data and models, J. Geophys. Res., 105, 767-780, https://doi.org/10.1029/1999JD901089, 2000.

Bessho, K., Date, K., Hayashi, M., Ikeda, A., Imai, T., Inoue, H., Kumagai, Y., Miyakawa, T., Murata, H., Ohno, T., Okuyama, A., Oyama, R., Sasaki, Y., Shimazu, Y., Shimoji, K., Sumida, Y., Suzuki, M., Taniguchi, H., Tsuchiyama, H., Uesawa, D., Yokota, H., and Yoshida, R.: An Introduction to Himawari-8/9 – Japan's New-Generation Geostationary Meteorological Satellite, J. Meteor. Soc. Jpn., 94, 151-183, https://doi.org/10.2151/jmsj.2016-009, 2016.

Boucher, O., Randall, D., Artaxo, P., Bretherton, C., Feingold, G., Forster, P., Kerminen, V.-M., Kondo, Y., Liao, H., Lohmann, U., Rasch, P., Satheesh, S., Sherwood, S., Stevens, B., and Zhang, X.: Clouds and Aerosols, book section 7, p. 571-658, Cambridge Univ. Press, Cambridge, UK and New York, https://doi.org/10.1017/CBO9781107415324.016, 2013.

Cess, R. D., Potter, G. L., Blanchet, J. P., Boer, G. J., Ghan, S. J., Kiehl, J. T., Treut, H. LE., Li, Z.-X., Liang, X.-Z., Mitchell, J. F. B., Morcrette, J.-J., Randall, D. A., Riches, M. R., Roeckner, E. R., Schles, U., Slingo, A., Taylor, K. E., Washington, W. W., Wetherald, R. T., and Yagai, I.: Interpretation of cloud-climate feedbacks as produced by 14 atmospheric general circulation model, Science, 245, 513-516, https://doi.org/10.1126/science.245.4917.513, 1989.

Chaboureau, J.-P., Tulet, P., and Mari, C.: Diurnal cycle of dust and cirrus over West Africa as seen from Meteosat Second Generation satellite and a regional forecast model, Geophys. Res. Lett., 34, LO2822, https://doi.org/10.1029/2006GL027771, 2007.

Chen, Y., Weng, F., Han, Y., and Liu, Q.: Validation of the community radiative transfer model by using CloudSat data, J. Geophys. Res., 113, D00A03, https://doi.org/10.1029/2007JD009561, 2008.

Chevallier, F., Lopez, P., Tompkins, A. M., Janiskova´, M., and Moreau, E.: The capability of 4D-Var systems to assimilate cloud-affected satellite infrared radiances, Q. J.. R. Meteorol. Soc. 130, 917-932, https://doi.org/10.1256/qj.03.113, 2004.

Cotton, W. R., Pielke, R. A. Sr., Walko, R. L., Liston, G. E., Tremback, C. J., Jiang, H., McAnelly, R. L., Harrington, J. Y., Nicholls, M. E., Carrio, G. G., and McFadden, J. P.: RAMS 2001: Current status and future directions, Meteor. Atmos. Phys., 82, 5-29, https://doi.org/10.1007/s00703-001-0584-9, 2003.

Dee, D. P., Uppala, S. M., Simmons, A. J., Berrisford, P., Poli, P., Kobayashi, S., Andrae, U., Balmaseda, M. A., Balsamo, G., Bauer, P., Bechtold, P., Beljaars, A. C. M., van de Berg, L., Kållberg, P., Kållber, M., Matricardi, M., McNally, A.

P., Monge-Sanz, B. M., Morcrette, J.-J., Park, B.-K., Peubey, C., de Rosnay, P., Tavolato, C., Thépaut, J.-N., and Vitart, F.: The ERA-Interim reanalysis: configuration and performance of the data assimilation system, Q. J. Roy. Metero. Soc., 127, 553-597, https://doi.org/10.1002/qj.828, 2011.

Ding, S., Yang, P., Weng, F., Liu, Q., Han, Y., van Delst, P., Li, J., and Baum, B.: Validation of the community radiative transfer model, J. Quant. Spectrosc. Radiat. Transf., 112, 1050-1064, https://doi.org/10.1016/j.jqsrt.2010.11.009, 2010.

Dufresne, J.-L., and Bony, S.: An assessment of the primary sources of spread of global warming estimates from coupled atmosphere-ocean model, J. Climate, 21, 5135-5144, https://doi.org/10.1175/2008JCLI2239.1, 2008.

Free, M., Sun, B., and Yoo, H. L.: Comparison between Total Cloud Cover in Four Reanalysis Products and Cloud Measured by Visual Observations at US Weather Stations, J. Climate, 29, 2015-2021, https://doi.org/10.1175/JCLI-D-15-0637.1, 2016.

Gelaro, R., McCarty, W., Suárez, M. J., Todling, R., Molod, A., Takacs, L., Randles, C. A., Bosilovich, M. G., Reichle, R., Wargan, K., Copy, L., Cullather, R., Draper, C., Akella, S., Buchard, V., Conaty,, A., da Silve, A. M., Gu, W., Kim, G.-K., Koster, R., Lucchesi, R., Merkova, D., Nielsen, J. E., Partyka, G., Pawson, S., Putman, W., Rienecker, M., Schubert, S. D., Sienkiewicz, M., and Zhao, B.: The modern-era retrospective analysis for research and applications, version 2 (MERRA-2), J. Climate, 30, 5419-5454, https://doi.org/10.1175/JCLI-D-16-0758.1, 2017.

Guan, L. and Wang, Z.: Objective determination of AIRS cloud mask using co-located MODIS cloud mask, Scientia Meteorological Sincia, 27, 516-521, 2007.

Han, M., Braun, S. A., Matsui, T., and Williams, C. R.: Evaluation of cloud microphysics schemes in simulations of a winter storm using radar and radiometer measurements, J. Geophys. Res., 118, 1401-1419, https://doi.org/10.1002/jgrd.50115, 2013.

Hansen, J. E. and Hovenier, J. W.: The doubling method applied to multiple scattering of polarized light, J. Quant. Spectrosc. Radiat. Transf., 11, 809-812, https://doi.org/10.1016/0022-4073(71)90057-4, 1971.

Hansen, J. E. and Travis, L. D.: Light scattering in planetary atmospheres, Space. Sci. Rev., 16, 527-610, https://doi.org/10.1007/BF00168069, 1974.

Hashino, T., Satoh, M., Hagihara, Y., Kubota, T., Matsui, T., Nasuno, T., and Okamoto, H.: Evaluating cloud microphysics from NICAM against CloudSat and CALIPSO, J. Geophys. Res., 118, 7273-7292, https://doi.org/10.1002/jgrd.50564, 2013.

Hersbach, H. and Dee, D.: “ERA5 reanalysis is in production”, ECMWF Nesletter, number 147, Spring 2016, p. 7, 2016.

Heymsfield, A. J., Matrosov, J. S., and Baum, B.: Ice water path optical depth relationships for cirrus and deep stratiform ice cloud layers, J. Appl. Meteor., 42, 1369-1390, https://doi.org/10.1175/1520-0450(2003)042<1369:IWPDRF>2.0.CO;2, 2003.

Heymsfield, A. J. and McFarquhar, G. M.: On the high albedos of anvil cirrus in the tropical Pacific warm pool: Microphysical interpretations from CEPEX and from Kwajalein, Marshall Islands, J. Atmos. Sci., 53, 2424-2451, https://doi.org/10.1175/1520-0469(1996)053<2424:HAOCIT>2.0.CO;2, 1996.

Holz, R. E., Ackerman, A., Nagle, F. W., Frey, R., Dutcher, S., Kuehn, R. E., Vaughan, M. A., and Baum, B.: Global Moderate Resolution Imaging Spectroradiometer (MODIS) cloud detection and height evaluation using CALIOP, J. Geophys. Res., 113, D00A19, https://doi.org/10.1029/2008JD009837, 2008.

Iwabuchi, H., Putri, N. S., Saito, M., Tokoro, Y., Sekiguchi, M., Yang, P., and Baum, B. A.: Cloud Property Retrieval from Multiband Infrared Measurements by Himawari-8, J. Meteor. Soc. Jpn., 96, 27-42, https://doi.org/jmsj.2018-001, 2018.

Jakob, C.: Cloud Cover in the ECMWF Reanalysis, J. Climate, 12, 947-959, https://doi.org/10.1175/1520-0442(1999)012<0947:CCITER>2.0.CO;2, 1999.

Järvinen, E., Jourdan, O., Neubauer, D., Yao, B., Liu, C., Andreae, M. O., Lohmann, U., Wendisch, M., McFarquhar, G. M., Leisner, T., and Schnaiter, M.: Additional global climate cooling by clouds due to ice crystal complexity, Atmos. Chem. Phys., 18, 15767-15781, https://doi.org.10.5194/acp-18-15767-2018, 2018.

Kalnay, E., Kanamitsu, M., Kistler, R., Collins, W., Deaven, D., Gandin, L., Iredell, M., Saha, S., White, G., Woolen, J., Zhu, Y., Chlliah, M,, Ebisuzaki, W., Higgins, W., Janowiak, J., Mo, K. C., Ropelewski, C., Wang, J., Leetmaa, A., Reynolds, R., Jenne, R., and Joseph, D.: The NCEP/NCAR 40-Year Reanalysis Project, Bull. Amer. Meteorol. Soc., 77, 1757-1774, https://doi.org/10.1175/1520-0477(1996)077<0437:TNYRP>2.0.CO;2, 1996.

King, M. D., Kaufman, Y. J., Menzel, W. P., and Tanre, D.: Remote sensing of cloud, aerosol, and water vapor properties from the Moderate Resoluting Imaing Spectrometer (MODIS), IEEE Trans. Geosci, Remote Sens., 301, 2-27, https://doi.org/10.1109/36.124212, 1992.

Kleist, D. T., Parrish, D. F., Derber, J. C., Treadon, R., Wu, W.-S., and Lord, S.: Introduction of the GSI into the NCEP Global Data Assimilation System, Wea. Forecasting, 24, 1691-1705, https://doi.org/10.1175/2009WAF2222201.1, 2009.

Kobayashi, S., Ota, Y., Harada, Y., Ebita, A., Moriya, M., Onoda, H., Onogi, K., Kamahori, H., Kobayashi, C., Endo, H., Miyaoka, K., and Takahashi, K.: The JRA-55 Reanalysis: General specifications and basic characteristics, J. Meteor. Soc. Jpn. Ser., 93, 5-48, https://doi.org/10.2151/jmsj.2015-001, 2015.

Lai, R., Teng, S., Yi, B., Letu, H., Min, M., Tang, S., and Liu, C.: Comparison of Cloud Properties from Himawari-8 and Fengyun-4A Geostationary Satellite Radiometers with MODIS Cloud Retrievals, Remote Sens., 11, 1703, https://doi.org/10.3390/rs11141703, 2019.

Liao, J., Hu, K., Jiang, H., Cao, J., Jiang, L., Li, Q., Zhou, Z., Liu, Z., Zhang, T., and Wang, H.: Pre-Process and Data Selection for Assimilation of Conventional Observations in the CMA Global Atmospheric Reanalysis, Advances in Met S&T., 8, 133-142, https://doi.org/10.2969/j.issn.2095-1973.2017.01.018, 2018.

Liu, Q., and Weng, F.: Advanced doubling-adding method for radiative transfer in planetary atmosphere, J. Atmos. Sci., 63, 3459-3465, https://doi.org/10.1175/JAS3803.1, 2006.

Mecikalski, J. R. and Bedka, K. M.: Forecasting convective initiation by monitoring the evolution of moving cumulus in daytime GOES imagery, Mon. Wea. Rev., 134, 49-78, https://doi.org/10.1175/MWR3062.1, 2006.

Mao, K., Qin, Z., Shi, J., and Gong, P.: A practical split-window algorithm for retrieving land-surface temperature from MODIS data, Int. J. Remote Sens., 26, 3181-3204, https://doi.org/10.1029/2006GL026547, 2005.

Matsui, T., Santanello, J., Shi, J. J., Tao, W.-K., Wu, D., Peters-Lidard, C., Kemp, E., Chin, M., Starr, D., Sekiguchi, M., and Aires, F.: Introducing multisensory satellite radiance-based evaluation for regional Earth System modeling, J. Geophys. Res., 119, 8450-8475, https://doi.org/10.1002/2013JD021424, 2014.

Mazin, I. P.: Cloud Phase Structure: Experimental Data Analysis and Parameterization, J. Atmos. Sci., 63, 667-681, https://doi.org/10.1175/JAS3660.1, 2004.

McNally, A. P.: The direct assimilation of cloud-affected satellite infrared radiances in the ECMWF 4D-Var, Q. J. R. Meteorol. Soc. 135, 1214-1229, https://doi.org/10.1002/qj.426, 2009.

Mie, G.: Beiträge zur optic trüber medien, speziell kolloidaler metallösungen, Ann. Phys., 330, 337-445, 1908.

Miles, N. L., Verlinde, J., and Clothiaux, E. E.: Cloud Droplet Size Distributions in Low-Level Stratiform Clouds, J. Atmos. Sci., 57, 295-311, https://doi.org/10.1175/1520-0469(2000)057<0295:CDSDIL>2.0.CO;2, 2000.

Morcrette, J.-J.: Evaluation of model-generated cloudiness: Satellite-observed and model-generated diurnal variability of brightness temperature, Mon. Wea. Rev., 119, 1205-1224, https://doi.org/10.1175/1520-0493(1991)119%3C1205:EOMGCS%3E2.0.CO;2, 1991.

Onogi, K., Tsutsui, J., Koide, H., Sakamoto, M., Kobayashi, S., Hatsushika, H., Matsumoto, T., Yamazaki, N., Kamahori, H., Takahashi, K., Kadokura, S., WADA, K., Kato, K., Oyama, R., Ose, T., Mannoji, N., and Taira, R.: The JRA-25 Reanalysis, J. Meteor. Soc. Jpn, 85, 369-432, https://doi.org/10.2151/jmsj.85.369, 2007.

Otkin, J. A., Greenwald, T. J., Sieglaff, J., and Huang, H.-L.: Validation of a large-scale simulated brightness temperature dataset using SEVIRI satellite observations, J. Climate, 25, 4975-4992, https://doi.org/10.1175/2009JAMC2142.1, 2009.

Platt, C. M. R.: A Parameterization of the Visible Extinction Coefficient of Ice Clouds in Terms of the Ice/Water Content, J. Atmos. Sci., 54, 2083-2098, https://doi.org/10.1175/1520-0469(1997)054<2083:APOTVE>2.0.CO;2, 1997.

Rienecker, M. M., Suarez, M. J., Gelaro, R., Todling, R., Bacmeister, J., Liu, E., Bosilovich, M. G., Schubert, S. D., Takacs, L., Kim, G.-K., Bloom, S., Chen, J., Collins, D., Conaty, A., da Silva, A., Gu, W., Joiner, J., Koster, R. D., Lucchesi, R., Molod, A., Owens, T., Pawson, S., Pegion, P., Redder, C. R., Reichle, R., Robertson, F, R., Ruddick, A. G., Sienkiewicz, M., and Woollen, J.: MERRA: NASA's Modern-Era Retrospective Analysis for Research and Applications, J. Climate, 24, 3624-3648, https://doi.org/10.1175/JCLI-D-11-00015.1, 2011.

Thompson, G., Rasmussen, R. M., and Manning, K.: Explicit forecasts of winter precipitation using an improved bulk microphysics scheme, Part I: Description and sensitivity analysis, Mon. Wea. Rev., 132, 519-542, https://doi.org/10.1175/1520-0493(2004)132%3C0519:EFOWPU%3E2.0.CO;2, 2004.

Twomey, S., Jacobowitz, H., and Howell, H. B.: Matrix methods for multiple-scattering problems, J. Atmos. Sci., 23, 289-298, https://doi.org/10.1175/1520-0469(1966)023%3C0289:MMFMSP%3E2.0.CO;2, 1966.

Uppala, S. M., KÅllberg, P. W., Simmons, A. J., Andrae, U., da costa Bechtold, V., Fiorino, M., Gibson, J. K., Haseler, J., Hernandez, A., Kelly, G. A., Li, X., Onogi, K., Saarinen, S., Sokka, N., Allan, R. P., Andersson, E., Arpe, K., Balmaseda, M. A., Beljaars, A. C. M, van de Berg, L., Bidlot, J., Bormann, N., Caires, S., Chevallier, F., Dethof, A., Dragosavac, M., Fisher, M., Fuentes, M., Hagemann, S., Hólm, E., Hoskins, B. J., Isaksen, L., Janssen, P. A. E. M.,

Jenne, R., Mcnally, A. P., Mahfouf, J.-F., Morcrette, J.-J., Rayner, N. A., Saunders, R. W., Simon, P., Sterl, A., Trenberth, K. E., Untch, A., Vasiljevic, D., Viterbo, P., and Woollen, J.: The ERA-40 re-analysis, Q. J. R. Meteorol. Soc., 131, 2961-3012, https://doi.org/10.1256/qj.04.176, 2005.

Wang, J., Liu, C., Min, M., Hu, X., Lu, Q., and Husi, L.: Effects and Applications of Satellite Radiometer 2.25-μm Channel on Cloud Property Retrievals, IEEE Trans. Geosci, Remote Sens., 56, 5207-5216, https://doi.org/10.1109/TGRS.2018.2812082, 2018.

Wang, M., Yao, S., Jiang, L., Liu, Z., Shi, C., Hu, K., Zhang, T., Zhang, Z., and Liu, J.: Collection and Pre-Processing of Satellite Remote-Sensing Data in CRA-40 (CMA's Global Atmospheric ReAnalysis), Advances in Met S&T., 8, 158-163, https://doi.org/10.3969/j.issn.2095-1973.2018.01.021, 2018.

Waliser, D. E., Li, J.-L. F., Woods, C. P., Austin, R. T., Bacmeister, J., Chern, J., Genio, A. D., Jiang, J. H., Kuang, Z., Meng, H., Minnis, P., Platnick, S., Rossow, W. B., Stephens, G. L., Sun-Mack, S., Tao, W.-K., Tompkins, A. M., Vane, D. G., Walker, C., and Wu, D.: Cloud ice: A climate model challenge with signs and expectations of progress, J. Geophys. Res., 114, D00A21, https://doi.org/10.1029/2008JD010015, 2009.

Weng, F.: A multi-layer discrete-ordinate method for vector radiative transfer in a vertically-inhomogeneous, emitting and scattering atmosphere: Theory. J. Quant. Spectrosc. Radiat. Transf., 47, 19-33, https://doi.org/10.1016/0022-4073(92)90076-G, 1992.

Wind, G., Da Silva, A. M., Norris, P. M., and Platnick, S.: Multi-sensor cloud retrieval simulator and remote sensing from model parameters-Part 1: Synthetic sensor radiance formulation, Geosci. Model Dev., 6, 2049-2062, https://doi.org/10.5194/gmd-6-2049-2013, 2013.

Wu, W. S., Purser, R. J., and Parrish, D. F.: Three-dimensional variation analysis with spatially inhomogeneous covariances, Mon. Wea. Rev., 130, 2905-2916, https://doi.org/10.1175/1520-0492(2002)130<2905:TDVAWS>2.0.CO;2, 2002.

Yang, P., Bi, L., Baum, B. A., Liou, K.-N., Kattawar, G. W., Mishchenko, M. I., and Cole, B.: Spectrally consistent scattering, absorption, and polarization properties of atmospheric ice crystals at wavelengths from 0.2 to 100 μm, J. Atmos. Sci., 70, 330-347, https://doi.org/10.1175/JAS-D-12-039.1, 2013.

Yang, P., Liou, K.-N., Bi, L., Liu, C., Yi, B., and Baum, B. A.: On the radiative properties of ice clouds: Light scattering, remote sensing, and radiation parameterization. Adv. Atmos. Sci., 32, 32-63, https://doi.org/10.1007/s00376-014-0011-z, 2015.

Yao, B., Liu, C., Yin, Y., Zhang, P., Min, M., and Han, W.: Radiance-based evaluation of WRF cloud properties over East Asia: Direct comparison with FY-2E observations, J. Geophys. Res., 123, 4613-4629, https://doi.org/10.1029/2017JD027600, 2018.

Yi, B., Yang, P., Liu, Q., van Delst, P., Boukabara, S.-A., and Weng, F.: Improvements on the ice cloud modeling capabilities of the Community Radiative Transfer Model, J. Geophys. Res., 121, 577-590, https://doi.org/10.1002/2016JD025207, 2016.

Yi, B., Rapp, A. D., Yang, P., Baum, B. A., and King, M. D.: A comparison of Aqua MODIS ice and liquid water cloud physical and optical properties between collection 6 and collection 5.1: Pixel-to-pixel comparisons, J. Geophys. Res., 122, 4528-4549, https://doi.org/10.1002/2016JD025586, 2017a.

Yi, B., Rapp, A. D., Yang, P., Baum, B. A., and King, M. D.: A comparison of Aqua MODIS ice and liquid water cloud physical and optical properties between collection 6 and collection 5.1: Cloud radiative effects, J. Geophys. Res., 122, 4550-4565, https://doi.org/10.1002/2016JD25654, 2017b.

Yu, W., Sèze, G., Treut, H. L., and Desbois, M.: Comparison of radiance fields observed by satellite and simulated by the LMD general circulation model. Dyn. Atmos. Oceans., 16, 147-165, https://doi.org/10.1016/0377-0265(91)90018-B, 1991.

Zhang, P., Lu, Q., Hu, X., Gu, S., Yang, L., Min, M., Chen, L., Xu, N., Sun, L., Bai, W., Ma, G., and Xian, D.: Latest progress of the Chinese Meteorological Satellite program and core data processing technologies, Adv. Atmos. Sci., 36, 1027-1045, 2019.

Zhou, G. and Gao, S.: Analysis of the September 2016 Atmospheric Circulation and Weather, Meteor. Mon., 42, 1560-1566, https://doi.org/10.7519/j.issn.1000-0526.2016.12.015, 2016.

Table 1. Geophysical parameters from the reanalysis datasets used in the evaluation.

Ordinal	Parameters
1	Temperature at surface
2	Pressure at surface
3	Cloud mixing ratio
4	Atmospheric profiles (pressure, specific humidity, and temperature profiles)

570

Table 2. Average ratios of cloud pixels for different layer clouds in Figure 10, and the average values of the mean BTDs (MBTD), standard deviation of BTDs (SBTD), and correlation coefficient (R) between the simulation and observation in Figure 12.

Cloud	All			Spring			Summer			Autumn			Winter		
	CRA	ERA5	MERRA-2	CRA	ERA5	MERRA-2	CRA	ERA5	MERRA-2	CRA	ERA5	MERRA-2	CRA	ERA5	MERRA-2
Total	0.99	1.14	1.27	1.00	1.15	1.29	0.99	1.16	1.32	0.98	1.14	1.25	1.01	1.12	1.22
Low	0.87	1.15	1.04	0.86	1.17	1.07	0.85	1.14	0.99	0.87	1.14	1.00	0.90	1.15	1.10
Mid	1.03	1.28	1.45	1.06	1.27	1.48	1.06	1.37	1.58	0.99	1.29	1.42	1.01	1.20	1.31
High	1.45	0.69	1.76	1.50	0.69	1.80	1.41	0.70	2.03	1.46	0.67	1.80	1.44	0.68	1.43

11.2-μm	All			Spring			Summer			Autumn			Winter		
	CRA	ERA5	MERRA-2	CRA	ERA5	MERRA-2	CRA	ERA5	MERRA-2	CRA	ERA5	MERRA-2	CRA	ERA5	MERRA-2
MBTD	-2.08	-0.92	-7.45	2.53	-0.89	-7.53	-2.08	-1.29	-9.58	-1.84	-0.94	-7.43	-2.07	-0.56	-5.26
SBTD	15.66	12.77	17.53	15.53	12.69	17.29	16.39	13.42	19.24	14.83	12.84	17.35	14.92	12.14	16.24
R	0.75	0.80	0.65	0.75	0.80	0.66	0.72	0.78	0.59	0.74	0.80	0.66	0.77	0.83	0.70

8.6-μm	All			Spring			Summer			Autumn			Winter		
	CRA	ERA5	MERRA-2	CRA	ERA5	MERRA-2	CRA	ERA5	MERRA-2	CRA	ERA5	MERRA-2	CRA	ERA5	MERRA-2
MBTD	-2.20	-1.68	-7.83	-2.44	-1.61	-7.86	-2.26	-2.17	-9.97	-1.93	-1.68	-7.80	-2.16	-1.27	-5.68
SBTD	14.98	12.16	16.75	14.82	12.07	16.48	15.70	12.79	18.36	15.14	12.25	16.62	14.27	11.53	15.54
R	0.75	0.81	0.65	0.75	0.81	0.66	0.73	0.78	0.59	0.74	0.80	0.66	0.77	0.83	0.70

6.2-μm	All			Spring			Summer			Autumn			Winter		
	CRA	ERA5	MERRA-2	CRA	ERA5	MERRA-2	CRA	ERA5	MERRA-2	CRA	ERA5	MERRA-2	CRA	ERA5	MERRA-2
MBTD	-0.78	0.78	-0.92	-0.83	0.75	-1.00	-0.85	0.73	-1.37	-0.70	0.82	-0.86	-0.73	0.84	-0.45
SBTD	4.43	3.78	5.05	4.36	3.68	4.94	4.53	3.96	5.54	4.41	3.80	4.98	4.40	3.67	4.75
R	0.87	0.90	0.82	0.87	0.90	0.82	0.87	0.89	0.79	0.87	0.90	0.83	0.88	0.91	0.86

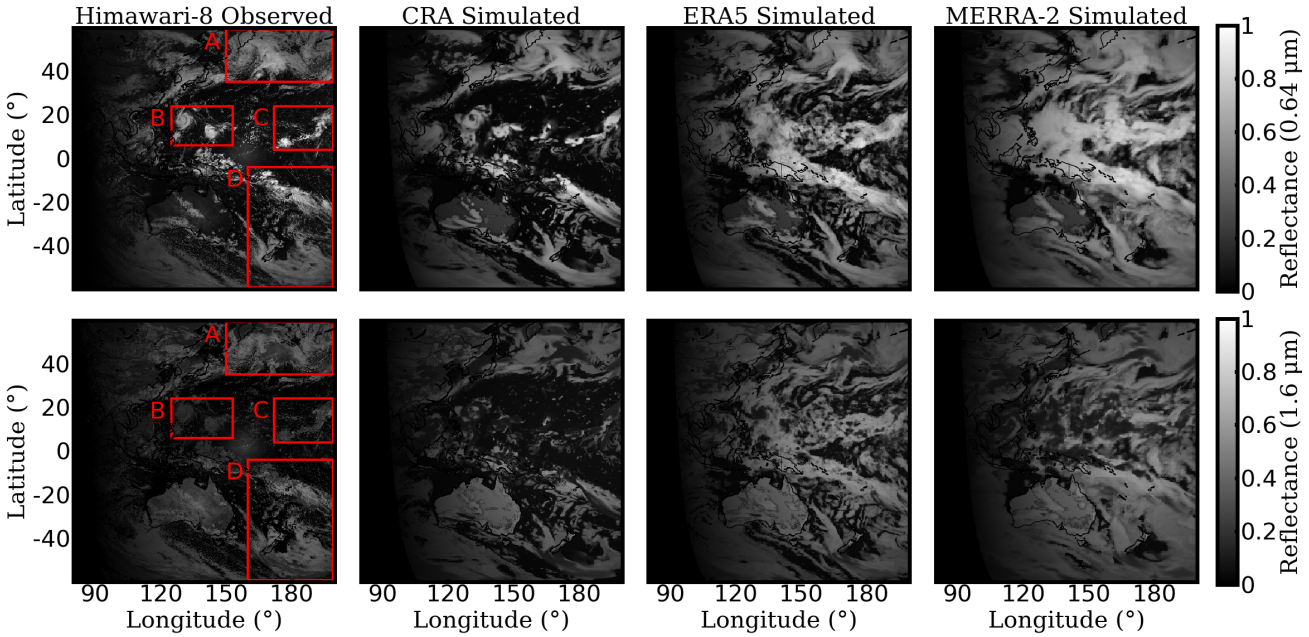

Figure 1. Observed and simulated reflectance in the 0.64-μm (top) and 1.6-μm (bottom) channels. The results are taken at 00:00 (UTC) on 12 September 2016.

580

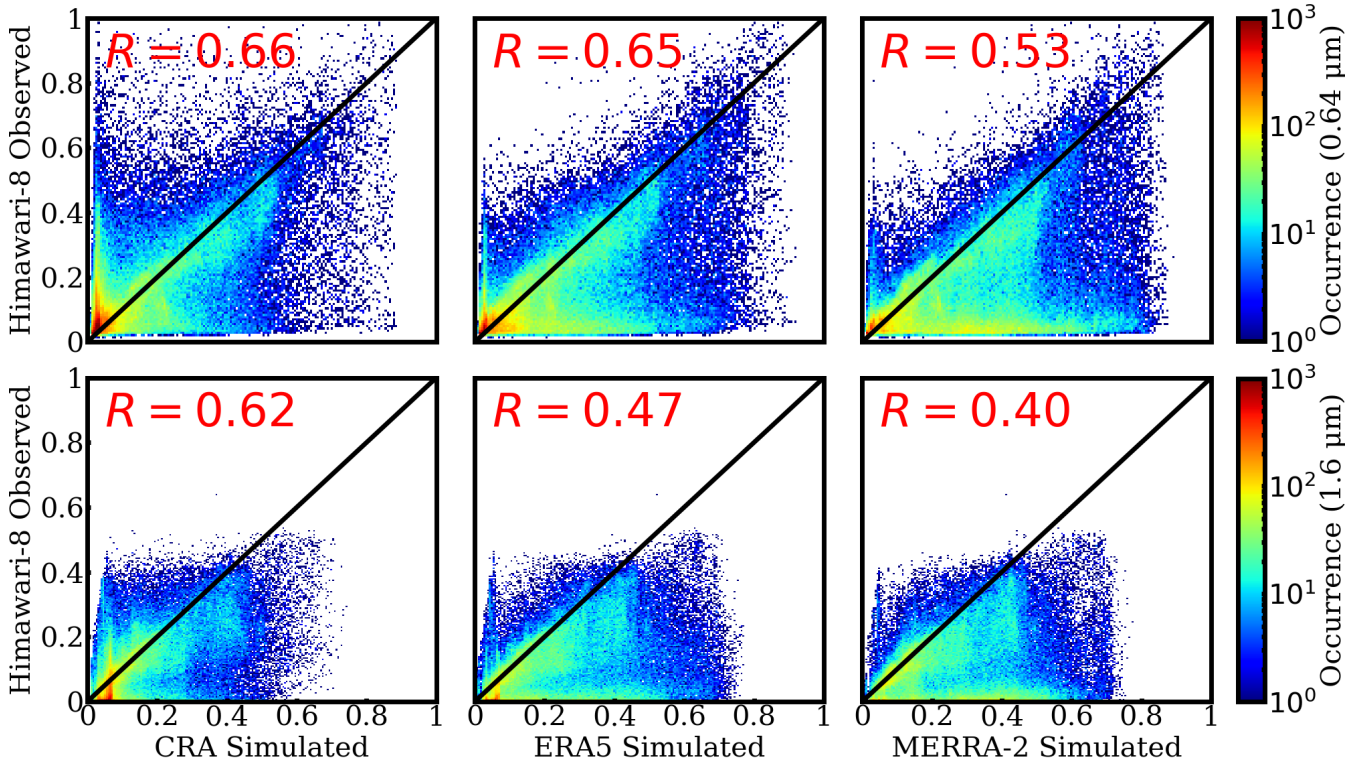

Figure 2. Pixel-to-pixel comparisons between the observed and simulated reflectance in the 0.64-μm (top) and 1.6-μm (bottom) channels. The histograms illustrate the occurrences of reflectance, and the results are taken at the same time as that in Figure 1.

585

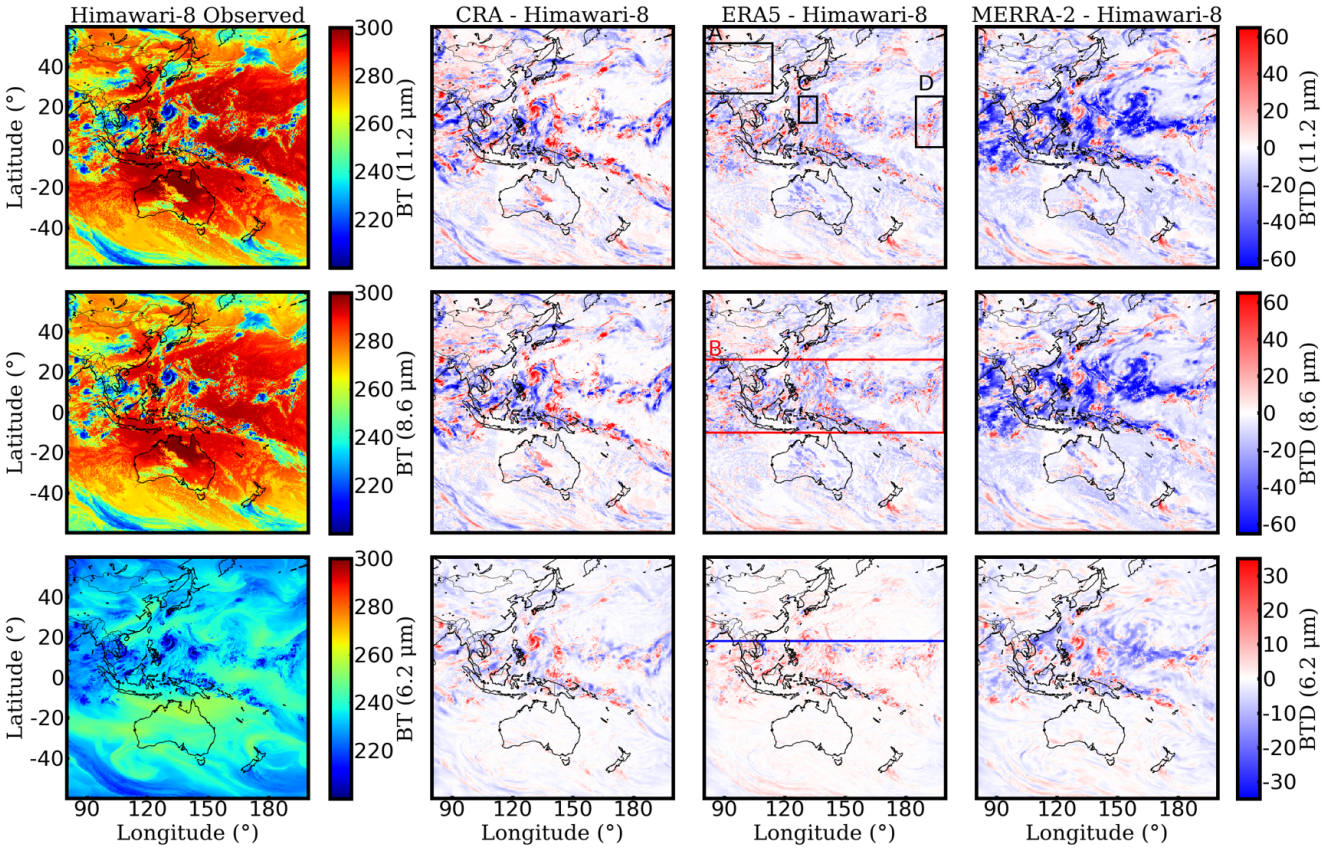

Figure 3. Observed results and the brightness temperature differences between the observations and simulations in the 11.2-μm (top), 8.6-μm (middle), and 6.2-μm (bottom) channels. The results are taken at the same time as that in Figure 1.

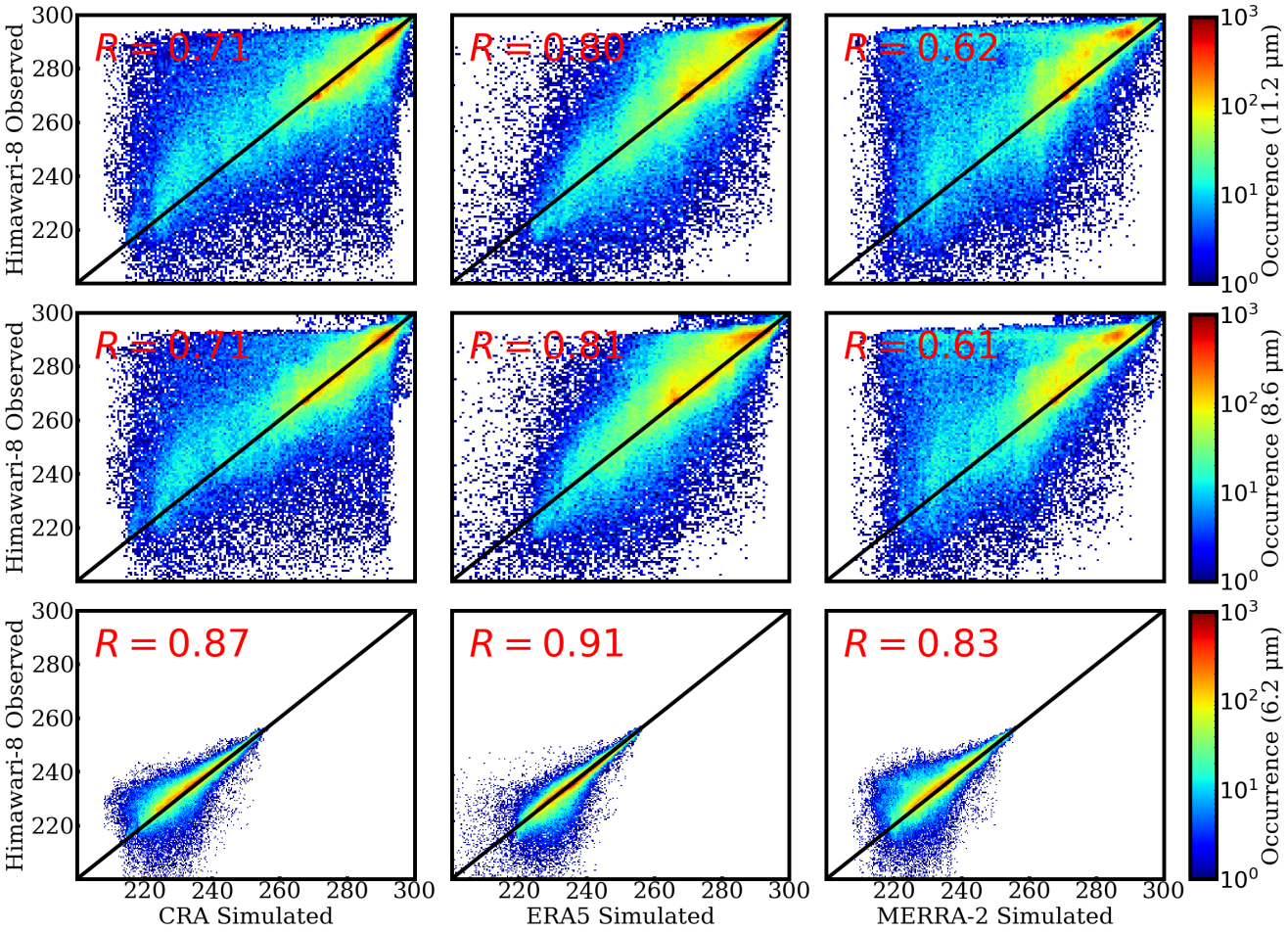

590

Figure 4. Same as the results in Figure 2, but for the infrared channels.

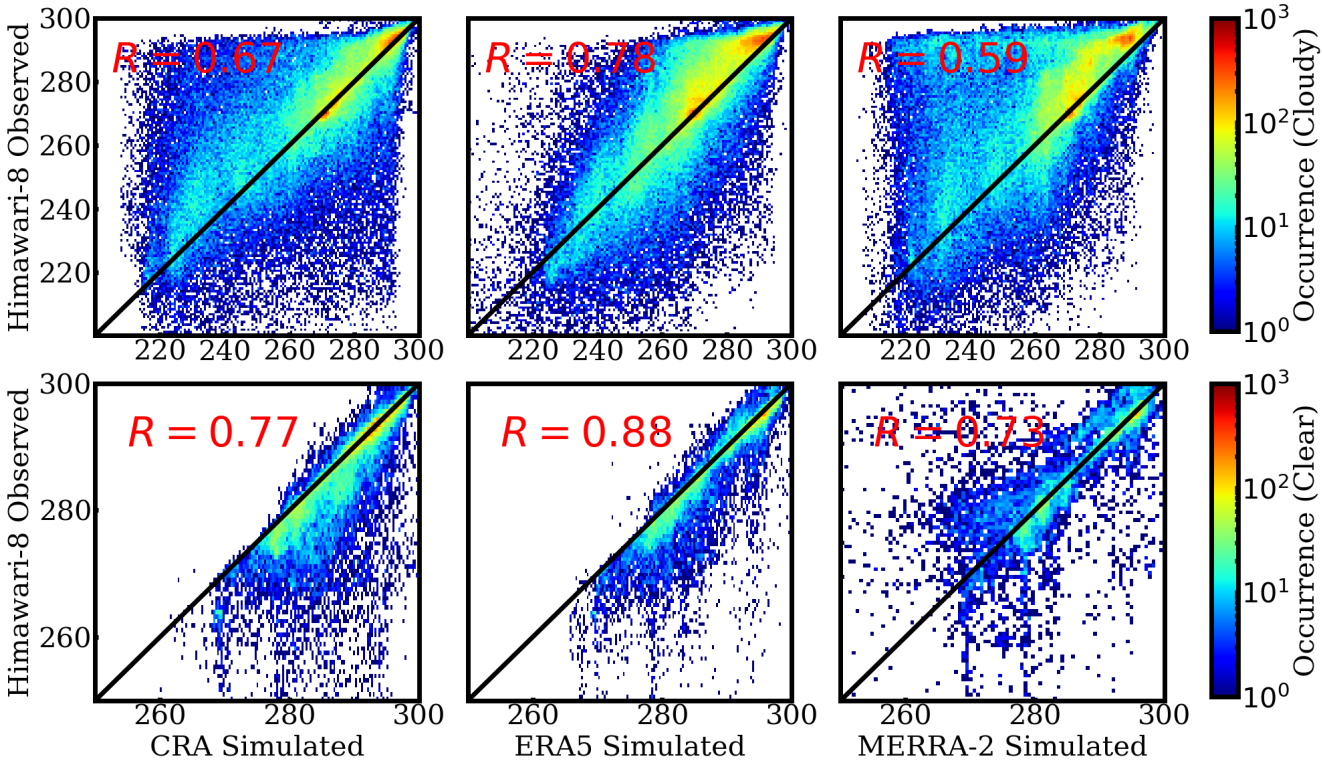

Figure 5. Comparisons between the observed and simulated BTs in the 11.2-μm channel for cloudy (top) and clear-sky pixels, respectively.

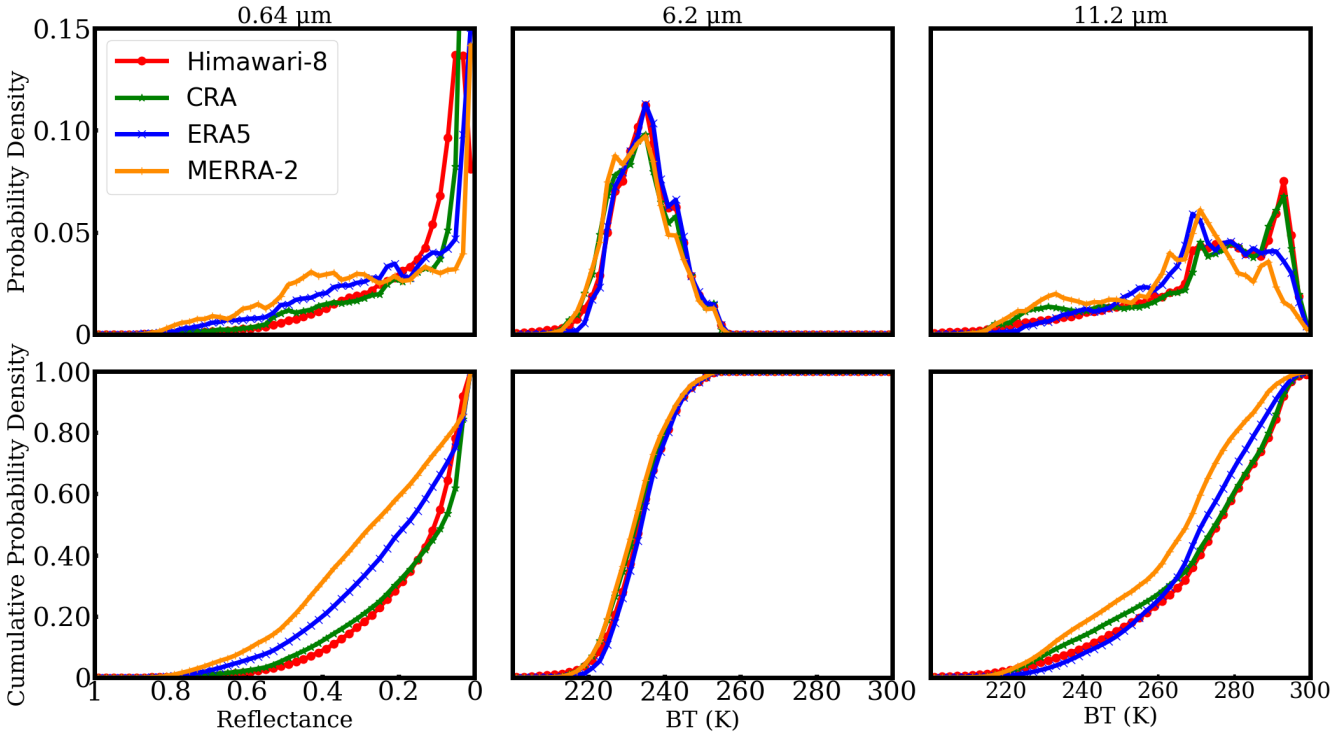

Figure 6. Probability and cumulative probability density for the observed and simulated reflectances in the 0.64-µm (left) channel and the BTs in the 6.2- (middle) and 11.2-µm (right) channels.

600

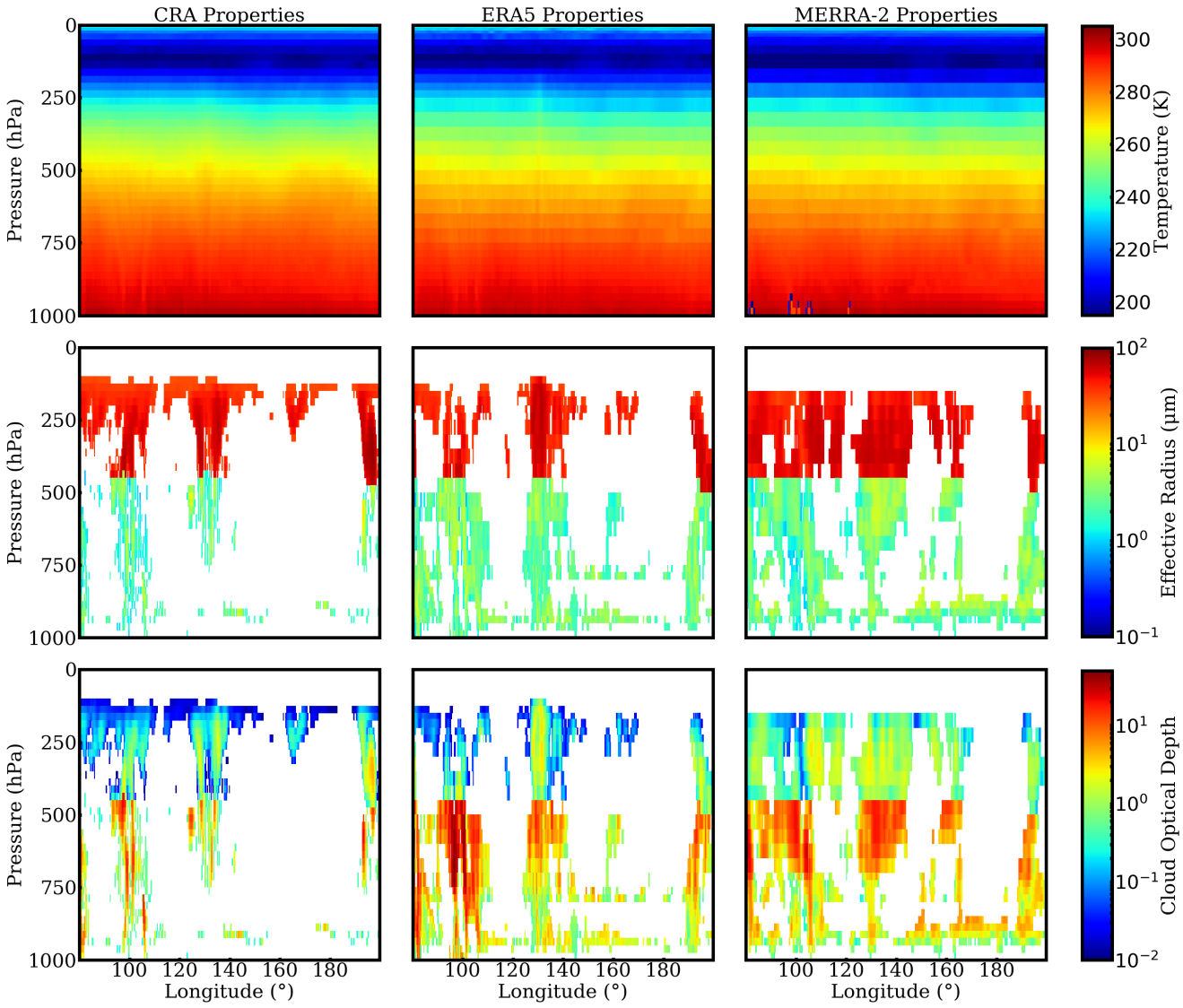

Figure 7. Comparison of the profiles of temperature, cloud effective radius and optical depth in CRA (left), ERA5 (middle), and MERRA-2 (right) reanalysis datasets. The profiles are for the track marked by blue solid lines in Figure 3.

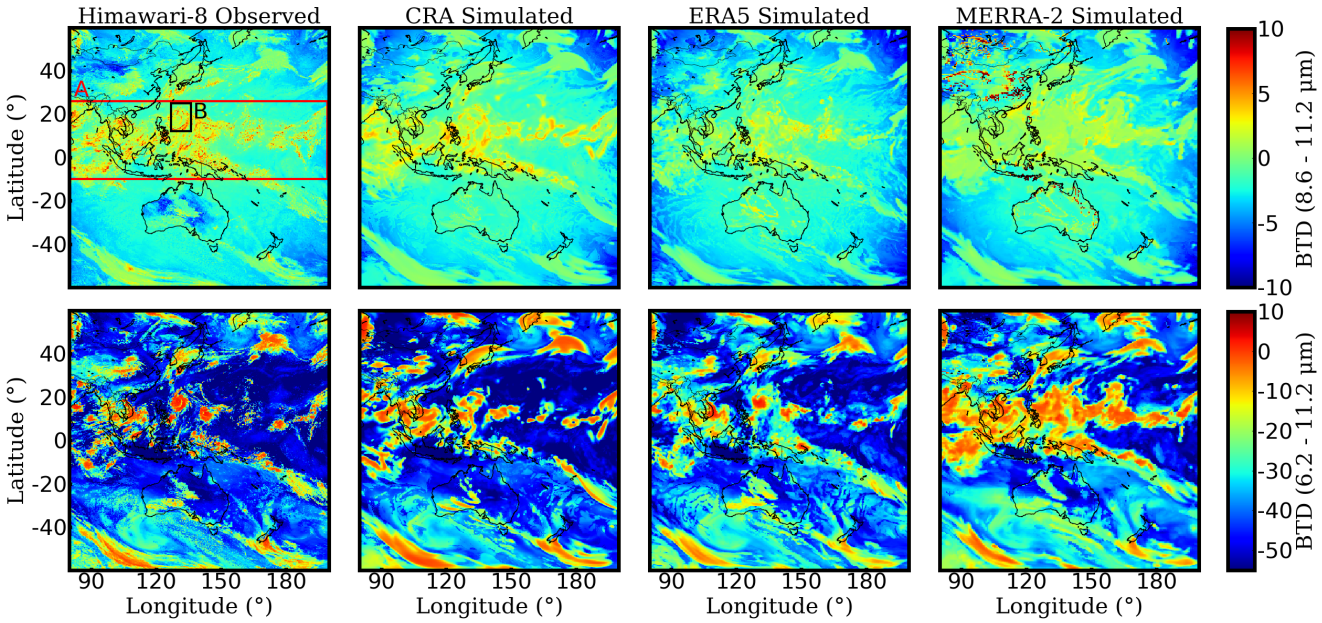

Figure 8. Observed and simulated brightness temperature differences of 8.6–11.2-μm (top) and 6.2–11.2-μm (bottom). The results are taken at the same time as that in Figure 1.

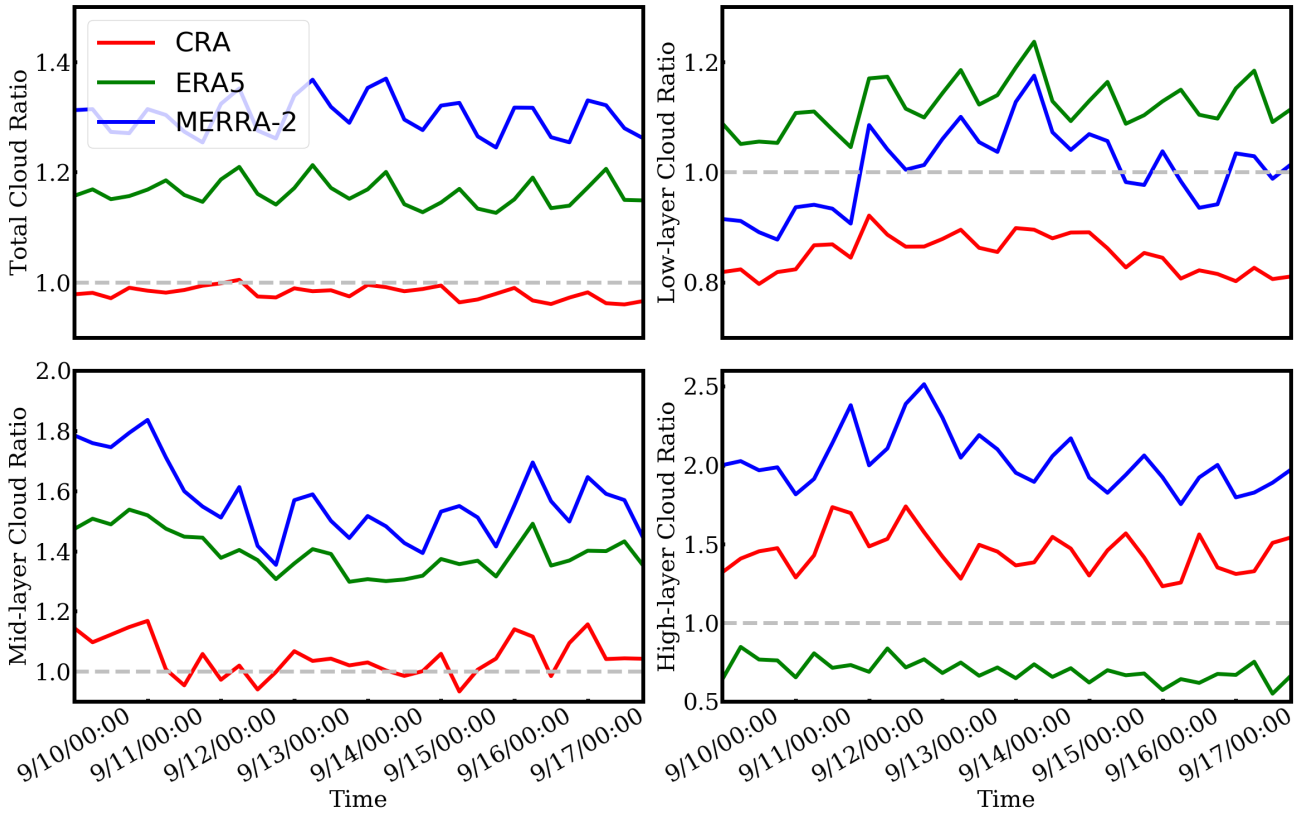

610 **Figure 9.** Temporal variation of the ratios (simulation-to-observation) for different layer clouds. The classification of clouds is based on the brightness temperature differences of 6.2–11.2-μm.

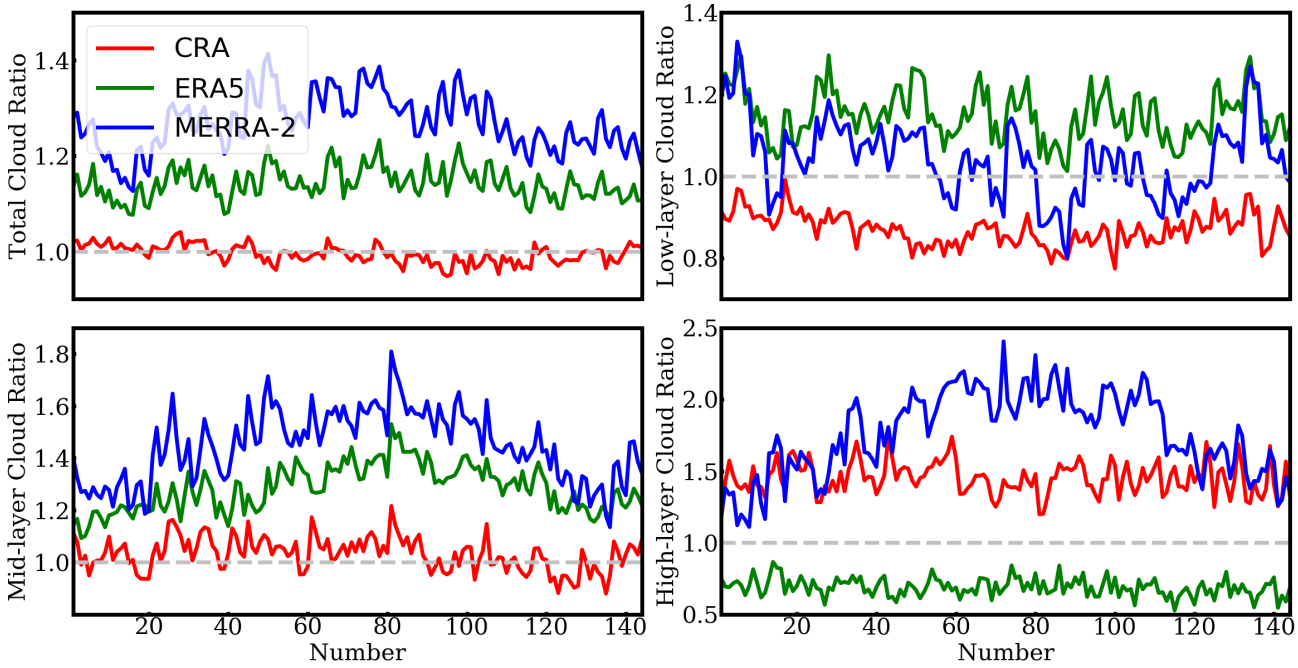

Figure 10. Same as Figure 9, but for the results from 144 realizations spanning over 2016.

615

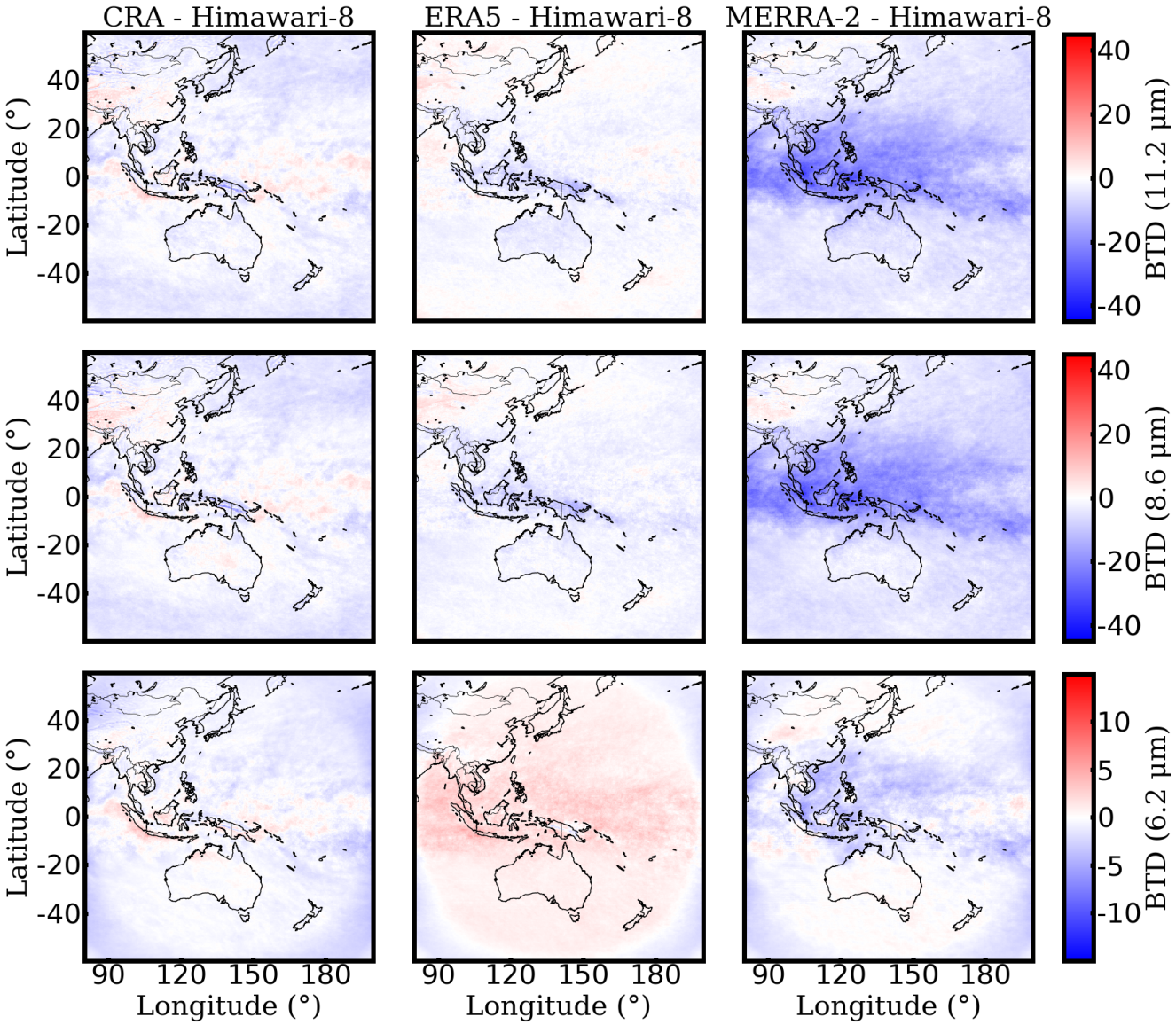

Figure 11. Average result of brightness temperature differences between the observation and simulation in the 11.2-μm (top), 8.6-μm (middle), and 6.2-μm (bottom) channels. The observation and simulation are from the 144 realizations spanning over 2016.

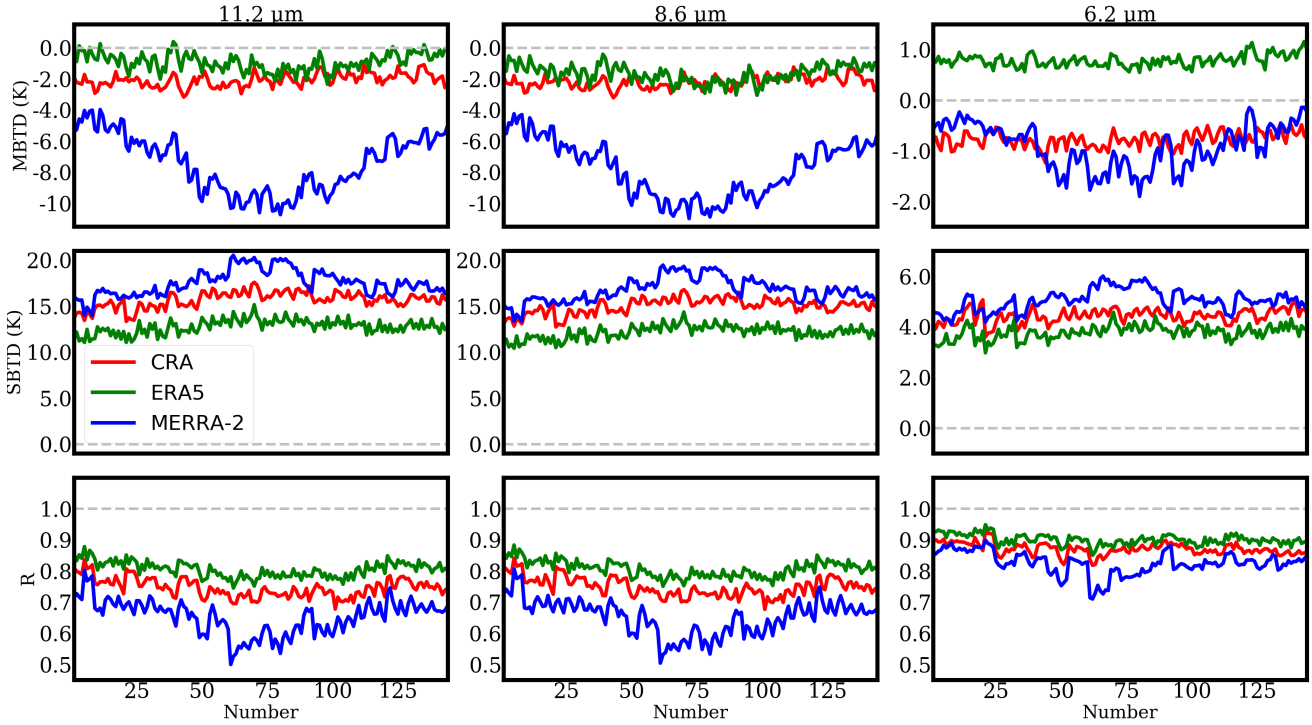

Figure 12. Temporal variation of three statistical parameters: the mean BTDs (MBTD), standard deviations of BTDs (SBTD), and correlation coefficient (R) between the simulation and observation. The results are from 144 realizations spanning over 2016.